Journal of Environmental Chemical Engineering xxx (xxxx) 111342

Contents lists available at ScienceDirect

Journal of Environmental Chemical Engineering

journal homepage: www.elsevier.com/locate/jece

Ultra-small Ni@NiFe2O4/TiO2 magnetic nanocomposites activated peroxymonosulphate for solar light-driven photocatalytic mineralization of Simazine

C. Ashina [a, 1], N. Pugazhenthiran [b, 1], P. Sathishkumar [a, *], M. Selvaraj [c, *], Mohammed A. Assiri [c], Chandrasekaran Rajasekaran [d], M.A. Gracia-Pinilla [e], R.V. Mangalaraja [f]

[a] Department of Chemistry, School of Advanced Sciences, Vellore Institute of Technology (VIT), Vellore, India
[b] Department of Chemistry, Universidad Técnica Federico Santa María, Av. España 1680, Valparaíso, Chile
[c] Department of Chemistry, Faculty of Science, King Khalid University, PO Box 9004, Abha 61413, Saudi Arabia
[d] Department of Biotechnology, School of Bio Sciences and Technology, Vellore Institute of Technology (VIT), Vellore, India
[e] Universidad Autonoma de Nuevo Leon, Facultad de Ciencias Físico-Matematicas, Av. Universidad, Cd. Universitaria, San Nicolas de los Garza, N.L., Mexico
[f] Faculty of Engineering and Sciences, Universidad Adolfo Ibanez, Diagonal Las Torres 2640, Santiago, Peñalolén, Chile

ARTICLE INFO

Keywords:
Simazine
Photocatalysis
Sonochemical approach
HPLC
Mineralization
Hydroxyl radicals

ABSTRACT

In the heterogeneous photocatalytic degradation of environmental contaminants the recovery and reuse of employed nanocatalyst was crucial and it is essentially required for the scale up applications. Besides, designing a magnetic material with heterojunction that can effectively oxidize the toxic organic contaminants to non-toxic substance under different reaction conditions including direct solar light irradiation remains a challenge. Considering the above facts, herein, we tailored heterojunction between the magnetic materials and non-magnetic materials with ultra-small Ni nanoparticles modified $NiFe_2O_4/TiO_2$ nanostructures ($Ni@NiFe_2O_4/TiO_2$ magnetic nanocomposites) through a simple sonochemical route. The Raman phonons at ~ 540 cm^{-1} consistent to nickel metal nanoparticles and the spinel ferrites crystal structure confirmed the formation of $Ni@NiFe_2O_4/TiO_2$ magnetic nanocomposites. The reduced optical bandgap of the resulting nanocomposites indicated the effective absorption of direct solar light irradiation when compared to the bare TiO_2. Thus in-turn, enhanced the photocatalytic efficiency of simazine degradation in the presence of $Ni@NiFe_2O_4/TiO_2$ magnetic nanocomposites ($k' = 11.0 \times 10^{-4}$ s^{-1}) and augmented the activation of peroxymonosulphate (PMS) in the presence of $Ni@NiFe_2O_4/TiO_2$ magnetic nanocomposites ($k' = 32.5 \times 10^{-4}$ s^{-1}). $Ni@NiFe_2O_4/TiO_2$ + PMS exhibited 3 folds enhanced efficiency in the presence of sunlight. The as-prepared $NiFe_2O_4/TiO_2$ magnetic nanocatalysts were more stable and the efficiency of simazine oxidation was approximately same for the continuous five cycles at the optimized experimental conditions. The $Ni@NiFe_2O_4/TiO_2$ magnetic nanocomposites preparation and the activation of PMS may promise the applications in an efficient wastewater treatment.

1. Introduction

Metal/metal oxide loaded semiconductor nanocatalysts significantly contributes to the field of environmental research since their presence as tunable semiconductor tends to introduce new hybrid energy levels [1–4]. New energy levels in the resulting nanocomposites essentially altered the optical band structure for superior utilization of solar energy photons [5,6]. However, higher loading of metal/metal oxide nanoparticles at semiconductor nanocomposites will act as recombination center [2,6–8]. Ultra-small nanoparticles presence at semiconductor nanocomposites expressively enhanced quantum efficiency of catalytic processes due to enhanced surface-to-volume ratio [9–12]. In addition, heterojunctions resulted from ultra-small nanoparticles and semiconductor nanocomposites noticeably prevented the charge-carrier recombination which in turn enhanced the population of effective hydroxyl radicals [9–12]. Hence, the degradation of environmental pollutants situated at/near to nanocatalyst's surface was enhanced in addi-

* Corresponding authors.
E-mail addresses: sathishkumar.p@vit.ac.in (P. Sathishkumar), mselvaraj@kku.edu.sa (M. Selvaraj).
[1] Equally contributed.

https://doi.org/10.1016/j.jece.2023.111342
Received 15 June 2023; Received in revised form 17 October 2023; Accepted 26 October 2023
2213-3437/© 20XX

tion to photo-bleaching resulted from heterogeneous photocatalytic microenvironment.

Further, the advantages of magnetic nanocomposites are (i) magnetic and non-magnetic composites can be synthesized by loading magnetic nanoferrites with tunable semiconductors; (ii) enhanced reutilization possibilities; (iii) secondary pollutions due to unsafe disposal of nanocatalysts can be prevented and (iv) reduces the capital investment required for nanocatalysts preparation [13–17]. Among various metal/metal oxide nanoparticles investigated in the field of environmental research, Ni and NiO_x nanoparticles predominantly contributes for degradation of various environmental contaminants [18–20]. To further progress the efficacy of nickel based nanocatalysts, Ni and NiO_x were combined with other transition metals/metal oxides which in-turn produced magnetic nanocomposites [21–23]. In addition, various combination of Ni with other transition metals/metal oxides structures were investigated, $NiFe_2O_4$ is the only ferrite with an inverted spinel structure which can be expressed as $(Fe^{3+})_A[Ni^{2+}Fe^{3+}]_BO_4{}^{2-}$. The tetrahedral (A) sites of the $NiFe_2O_4$ structure are occupied by ferric ions, and the octahedral (B) sites are occupied by ferric ions and nickel ions [24]. Besides, nickel ferrite nanoparticles ($NiFe_2O_4$ NPs) have received much attention for photocatalytic applications owing to its high photochemical stability, magnetically separable, and magneto crystalline anisotropy [24,25]. However, lower bandgap of $NiFe_2O_4$ (1.53 eV) is limited its catalytic efficiency due to the instability. Various attempts have been made in the literature to enhance catalytic efficiency and to preserve magnetic properties of $NiFe_2O_4$ [26–29]. The hybridization of magnetic-non-magnetic materials efficiently improved heterogeneous catalytic efficacy and retained their magnetic features [21,22,24,30].

Activation of peroxymonosulfate (PMS) in the heterogeneous photocatalytic oxidation system have been constructed to strengthen the separation of photo-generated electrons and holes during photocatalytic processes. Therefore, the synergistic participation of electrons and holes has been fostered in order to improve the organic pollutant oxidation performance [31–35]. $NiFe_2O_4$ show excellent PMS activation ability by the co-existence of Ni^{2+} and Fe^{3+} in its molecular structure [36]. Recent investigations [36–38], indicate that the photocatalytic performance of $NiFe_2O_4$ is significantly improved by the addition of peroxymonosulphate (PMS). Similarly, the results suggest that TiO_2 is one of the best catalysts for the heterogeneous activation of PMS for the oxidation of organic pollutants [31–33]. Therefore, the hybridization of $NiFe_2O_4$ and TiO_2 would expect to demonstrate superior photocatalytic activation of PMS in the aqueous systems. Further, there are still no experimental evidence related to the activation of PMS by ultra-small Ni NPs modified $NiFe_2O_4/TiO_2$($Ni@NiFe_2O_4/TiO_2$) heterojunction interface, nor a surface reaction mechanism to describe the photocatalytic oxidation that takes place under direct solar light irradiation.

Simazine (2-chloro-4,6-bis(ethylamino)-s-triazine) is a chemically synthesized pesticide which is being utilized as second largest pesticide in agriculture lands since 1956. The specific mechanism of simazine is to control the pest in agricultural crops nevertheless only 0.1% efficiency is achieved, and the presence of remaining simazine leads to the total environmental pollution [39–41]. The presence of simazine in the aquatic environment declines the growth of zooplankton which is a major threat to the ecosystem. Hence, triazine flavored pesticides certainly required complete mineralization from the total environment to avoid the various detrimental effects of pesticides.

Herein, we demonstrated the preparation of ultra-small Ni nanoparticles decorated $NiFe_2O_4$ nanostructure, followed by $Ni@NiFe_2O_4/TiO_2$ magnetic nanocomposites using the commercially available ultrasonic piezoelectric transducer at low-frequency ultrasound (42 kHz; laboratory model). Further, the ultra-small Ni NPs and formed heterojunction between $Ni@NiFe_2O_4$ and TiO_2 through its lattice fusion were identified by high-resolution transmission electron microscopy (HR-TEM). The photocatalytic efficiency along with magnetic feature of ultra-small $Ni@NiFe_2O_4/TiO_{2\ heterojunction}$ magnetic nanocomposites were evaluated through the kinetic degradation of simazine in direct solar light irradiation. Additionally, the charge transfer was further accelerated to enhance photocatalytic activity by adding PMS as an external electron acceptor. The magnetic $Ni@NiFe_2O_4/TiO_2$ nanocomposites were separated from photocatalytic microenvironment with the assistance of external magnet and reuse for the photocatalytic experiments. Furthermore, total organic carbon analysis allows to identify the degree of mineralization of simazine. Finally, a surface reaction mechanism was proposed.

2. Experimental

2.1. Materials

Titanium dioxide nanopowder (TiO_2; 25 nm average diameter), nickel nitrate ($Ni(NO_3)_2{\cdot}6\,H_2O$) (99.999% trace metals basis) and ferric nitrate ($Fe(NO_3)_3{\cdot}9\,H_2O$) (99.999% trace metals basis) were purchased from the Sigma–Aldrich and used as starting material for the preparation of $NiFe_2O_4$ and $NiFe_2O_4/TiO_2$ nanocatalysts. Simazine ($C_7H_{12}ClN_5$; PESTANAL®, analytical standard) was received from Sigma–Aldrich and used without further purification. Unless otherwise specified, all reagents used were of analytical grade and the solutions were prepared using double distilled water.

2.2. Preparation of the nanocatalysts

The $NiFe_2O_4$ and $NiFe_2O_4/TiO_2$ nanocomposites were synthesized based on our previous publication [42] as follows, calculated amount of nickel nitrate and ferric nitrate precursor solutions were prepared separately and mixed under vigorous stirring. To the metal nitrate mixture, 2 g of TiO_2 nanopowder previously calcined at 400 °C was added in small portions with magnetic stirring and simultaneously the suspension was irradiated with ultrasound (42 kHz ultrasonic cleaner, power sonic 400 series). To the suspension of TiO_2, 50 mL of 2 N NaOH was added drop-by-drop with ultrasound irradiation and stirring. The ultrasonic irradiation was continued for one hour with circulation of water to maintain the room temperature. After ultrasonic irradiation, heterogeneous suspension was stirred continuously at room temperature for two hours. The nanocatalysts were collected by filtration (0.45 μm Nylon filter membranes) and washed with double-distilled water until the pH of the eluent reaches 7. The solids were dried at 100 °C in a hot air-oven for 12 h followed by calcination at 400 °C for 5 h to get pure nanocatalysts. A similar procedure was adopted for the synthesis of $NiFe_2O_4$ nanocatalysts for comparison. It is expected that the decorated nickel nanoparticles will significantly contribute to enhance quantum efficiency of magnetic nanocomposites.

2.3. Characterization techniques

The particle size of the prepared nanoparticles was calculated from the X-ray diffraction data (Philips PW1710 diffractometer, Cu-K_α radiation, Holland) using the Scherer equation. Surface morphology, grain size, and various contours of the nanocatalyst powders were analyzed by the transmission electron microscopy (FEI TITAN G² 80–300) operated at 300 KeV. Diffuse reflectance UV–vis spectra of the nanocatalysts were recorded using a Shimadzu 2550 spectrophotometer equipped with an integrating sphere accessory employing $BaSO_4$ as reference material. Raman spectra were recorded using a Raman in via model (Renishaw, UK) spectrometer, operating wavelength at 785 nm with a resolution of 1 cm^{-1}. The magnetization measurements were performed with the Quantum design PPMS-II (physical property measurement system) at the ambient conditions.

2.4. Evaluation of photocatalytic activity

The photocatalytic oxidation experiments were conducted under direct solar light irradiation in ambient atmospheric conditions in the month from September to April in the Chile. The geographic coordinates are 36° 47′ 50″ S; 71° 03′ 21″ W. All experiments were conducted with the exposition of the photocatalytic reactor to solar light between 11 AM to 4 PM. The intensity of incident solar irradiation, temperature and pH were measured during the elapsed irradiation time using an Extech instrument from USA, resulting to be constant with a value of 1,23,500 ± 10 lux, 22–25 °C and pH 7.0–6.7, respectively. A borosilicate stirred batch slurry reactor (Ø = 100 mm) was used, loaded with 150 mL solution of simazine (6.2 mg/L), and 0.3 g/L of the synthesized nanophotocatalyst. In a typical experiment, prior to irradiation adsorption/desorption equilibrium was achieved after 45 min of agitation in dark condition. After that the reactor was exposed to direct solar light irradiation. Sampling was conducted at specific time intervals by taking aliquots. Before any analytical measuring, samples were filtered using a 0.2 μm polyvinylidene fluoride (PVDF) filter. In addition, the influence of different factors such as catalyst dosage, PMS concentration, pH, inorganic ions (Cl^-, NO_3^-, HCO_3^- and $H_2PO_4^-$) and different water matrix on SZN degradation was assessed. The pH value was adjusted with nitric acid (0.1 M) and sodium hydroxide (0.1 M) solutions. The stability and reusability studies of the synthesized nanocatalyst with the highest photocatalytic activity were assessed during 60 min of light irradiation. After each treatment, the catalyst was magnetically recovered and washed with double distilled water thrice and then used in the subsequent experiments. For each operating cycle, a fresh solution of simazine was added into the reaction system.

2.5. Detection of simazine (SZN) and its oxidation by-products

The evolution of SZN and its oxidation by-products were monitored as a function of time by liquid chromatography using a HPLC analyzer (Shimadzu Prominence-i LC-2030 C 3D Plus) equipped with a photodiode-array detector (PDA) at λ_{max} = 222 nm. A Brownlee analytical C_{18} column (250 mm × 4.6 mm, 5 μm particle size) and a mobile phase constituted of acetonitrile-water system (60:40) were used for the separation. The injection volume was 10 μL and the flow rate was 1 mL min^{-1}. The calibration curve for SZN was constructed using the peak areas of standard samples of known concentration ranging between 0.01 and 6.2 mg/L with a correlation coefficient of R^2 = 0.9999.

The photocatalytic mineralization of SZN was followed by total organic carbon analysis (TOC) and was calculated using Eq. (1), as follows:

$$\text{SZNMineralisation}\,(\%) = \frac{TOC_0 - TOC_t}{TOC_0} \times 100 \quad (1)$$

where TOC_0 represents the TOC measured after reaching the adsorption equilibrium between SZN and the nanocatalyst; whereas TOC_t denotes the TOC concentration at a specific irradiation time. Samples were analyzed by direct injection of filtered solutions into a TOC analyzer (Shimadzu TOC-V_{CPH} model). Prior to the analysis, the instrument was calibrated with potassium hydrogen phthalate.

2.6. Identification of reactive species

The capacity of the synthesized heterojunction nanocatalysts to promote radical generation in photocatalytic experiments in the absence of SZN was quantified using fluorescence spectroscopy (FLS) in a Perkin Elmer fluorometer. Terephthalic acid (TA) was used as a probe molecule. In such experiments, the concentration of TA and catalyst were kept in 5 × 10^{-4} M and 0.3 g/L, respectively. The samples were excited at 315 nm and the change in the fluorescence (FL) intensity of 2-hydroxy terephthalic acid (HTA) was measured at λ_{max} = 425 nm. The formation of HTA is directly related to the amount of •OH radicals produced [9,33,43,44]. A calibration curve made by known concentrations of 2-hydroxy terephthalic acid was used for indirect quantification of •OH radicals. Additionally, the contribution of major radical species involved during photocatalytic oxidation of SZN using $NiFe_2O_4/TiO_2$ with and without the addition of PMS was determined. In these experiments, tertiary-butylalcohol (TBA) was used as a quencher of •OH radicals under specific operating conditions: [catalyst] = 0.3 g/L, [SZN] = 6.2 mg/L, [PMS] = 0.4 mM, [TBA] = 0.3 M [32]. The experiments were carried out during 60 min of direct solar light irradiation for $NiFe_2O_4/TiO_2$ + SZN + TBA combination and during 15 min of direct solar light irradiation for $NiFe_2O_4/TiO_2$ + SZN + PMS + TBA combination.

3. Results and discussion

3.1. Characterization of nanocatalysts

The transmission electron microscopic (TEM) images of $NiFe_2O_4/TiO_2$ are shown in Fig. 1a and b. The hexagonal, cuboid, rectangular and various shaped nanoparticle morphologies are observed for $NiFe_2O_4/TiO_2$. The distribution of black patches observed from the TEM micrographs signifies the fine distribution of $NiFe_2O_4$ nanoferrites on the surface of TiO_2. The darker patches over $NiFe_2O_4/TiO_2$ magnetic nanocomposites indicate the presence of ultra-small nickel nanoparticles. An average grain size of the $Ni@NiFe_2O_4/TiO_2$ magnetic nanocomposites was calculated ~ 18 nm from the TEM analysis. The high angle annular dark field (HAADF) scanning transmission electron microscopy (STEM) micrograph shown in Fig. 1c further supports the formation of various shaped $NiFe_2O_4/TiO_2$ magnetic nanocomposites and the bright emission observed from HAADF-STEM indicates the ultra-small Ni metal nanoparticles were finely decorated on $NiFe_2O_4/TiO_2$ magnetic nanocomposites however it needs further analysis for confirmation. The SAED pattern observed for $NiFe_2O_4/TiO_2$ magnetic nanocomposites is displayed in Fig. 1d. The distinct rings with specific space between rings indicated well-crystalline nature of $NiFe_2O_4/TiO_2$ magnetic nanocomposites.

The high resolution TEM analysis of $NiFe_2O_4/TiO_2$ magnetic nanocomposites confirms the presence of lattice fringes corresponding to Ni (1 1 1), $NiFe_2O_4$ (2 1 1) and TiO_2 (0 0 2) as evidenced from Fig. 2a and b. In addition, black patches detected over $NiFe_2O_4$ crystal plane confirms that ultra-small Ni nanoparticles were embedded at the surface of $NiFe_2O_4/TiO_2$ magnetic nanocomposites. Heterojunction of various crystal planes were noticed from Fig. 2a which designates that Ni nanoparticles embedded at the surface of $NiFe_2O_4/TiO_2$ magnetic nanocomposites, the presence of Ni nanoparticles significantly contribute to delay the recombination of electronic charges produced at the interface during its applications. Furthermore, the circled portions of Fig. 2c and d indicate the presence of ultra-small Ni nanoparticles at grain boundaries of $NiFe_2O_4/TiO_2$ magnetic nanocomposites with average grain size ranging from 0.15 to 0.24 nm. Consequently, the presence of ultra-small Ni nanoparticles at grain boundaries of $NiFe_2O_4/TiO_2$ magnetic nanocomposites tends to specify the formation of new energy levels at resulting magnetic nanocomposites and it will alter the optical band structure [45,46].

Magnetization-hysteresis (M-H) loops recorded at room temperature during VSM analysis for as-prepared magnetic nanocomposites is presented in Fig. 3. Bare $Ni@NiFe_2O_4$ nanoferrites exhibiting soft ferromagnetic nature with magnetic saturation (Ms) value of 27 emu/g which is relatively lower than the observed theoretical value (Ms = 56 emu/g) [22,24,28,36,47]. The observed decrease in magnetization value is associated with various factors like surface spin and anisotropy of $Ni@NiFe_2O_4$ magnetic nanoferrites [22,24,25,28,36,39,48]. However, bare TiO_2 cannot show any significant changes during VSM analysis. M-H loops observed for $NiFe_2O_4/TiO_2$ magnetic nanocomposites

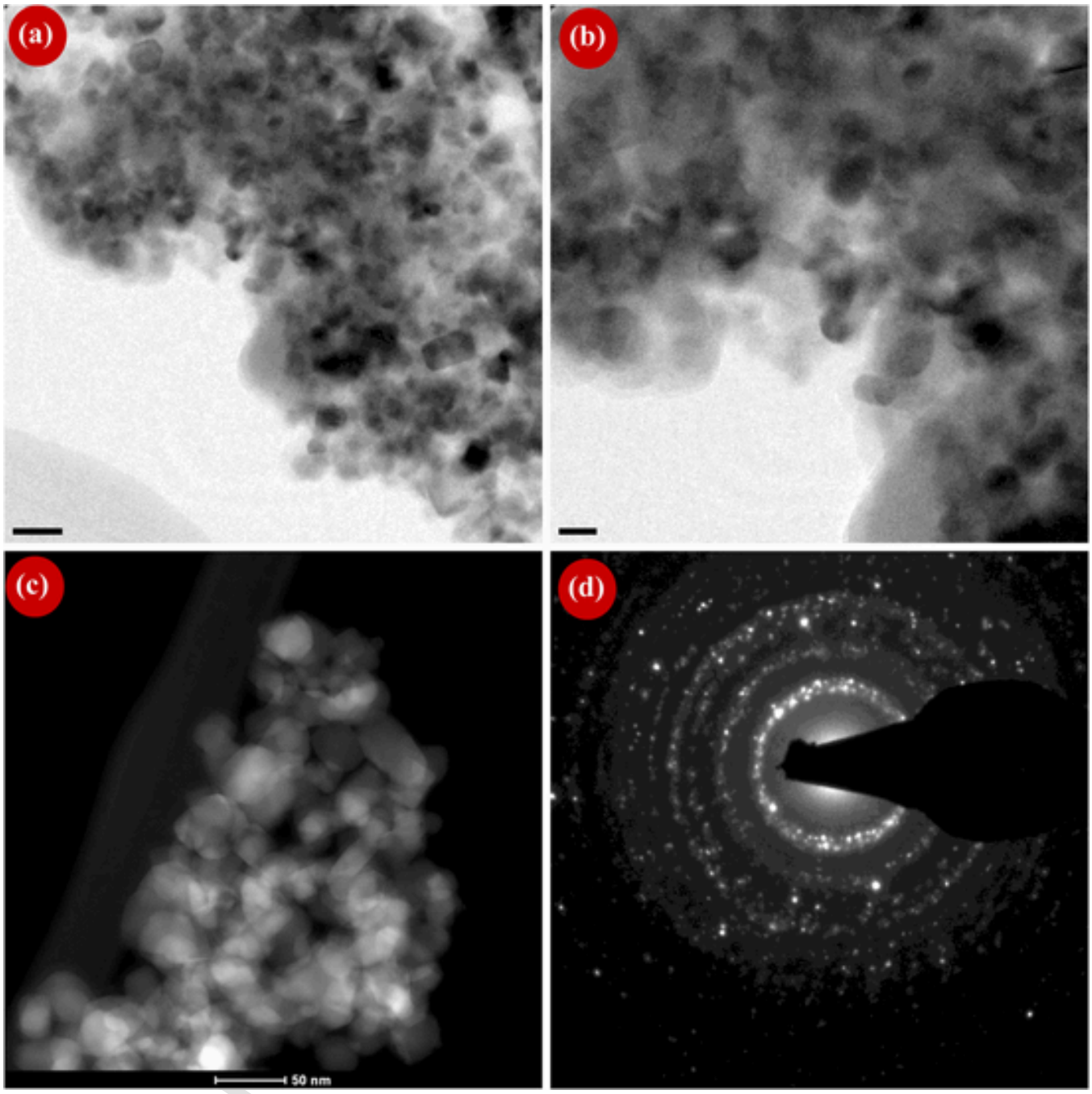

Fig. 1. TEM micrographs of Ni@$NiFe_2O_4$/TiO_2 magnetic nanocomposites (a & b); (c) HAADF-STEM image of Ni@$NiFe_2O_4$/TiO_2 magnetic nanocomposites and corresponding SAED pattern (d).

was shown in insert of Fig. 3. Ms value of Ni@$NiFe_2O_4$ was decreased when the nanoferrites are hybridized with TiO_2 since non-magnetic layer acts as dead layer during VSM analysis. On the other hand, TiO_2 magnetic characteristics was meaningfully improved with modification of Ni@$NiFe_2O_4$ magnetic nanoferrites. The resulting magnetic nanocomposites can be separated from photocatalytic microenvironment with assistance of external magnet and recycled for checking re-utilization of Ni@$NiFe_2O_4$/TiO_2 magnetic nanocomposites.

The X-ray diffraction pattern (XRD) of as-prepared magnetic nanocomposites is depicted in Fig. 4. The diffraction pattern belonging to TiO_2 shown pristine crystal structure with anatase (80%) and rutile (20%) polymorphs (JCPDS card no. 21–1272). Ni@$NiFe_2O_4$/TiO_2 magnetic nanocomposites also revealed pristine TiO_2 crystal structure with standard anatase-rutile ratio which denotes that crystal structure of TiO_2 is not altered during the synthesis of magnetic nanocomposites (Fig. 4). Furthermore, crystal planes belonging to $NiFe_2O_4$ (JCPDS card no. 10–0325) were detected in $NiFe_2O_4$/TiO_2 nanocomposites confirms the loading of spinel magnetic nanoferrites into TiO_2. The protracted diffraction pattern of spinel magnetic nanoferrites suggests poor crystalline nature of $NiFe_2O_4$ (Fig. 4). The insert of Fig. 4 comparatively validates the modifications occurred at TiO_2 during $NiFe_2O_4$ loading by low-frequency ultrasound assisted technique followed by calcination. In addition to the diffraction planes of $NiFe_2O_4$, diffraction belonging to nickel metal nanoparticles (JCPDS card nos. 04–0850) were detected (insert of Fig. 4). The observed crystal planes of nickel nanoparticles along with $NiFe_2O_4$ confirms the formation of Ni@$NiFe_2O_4$ which is

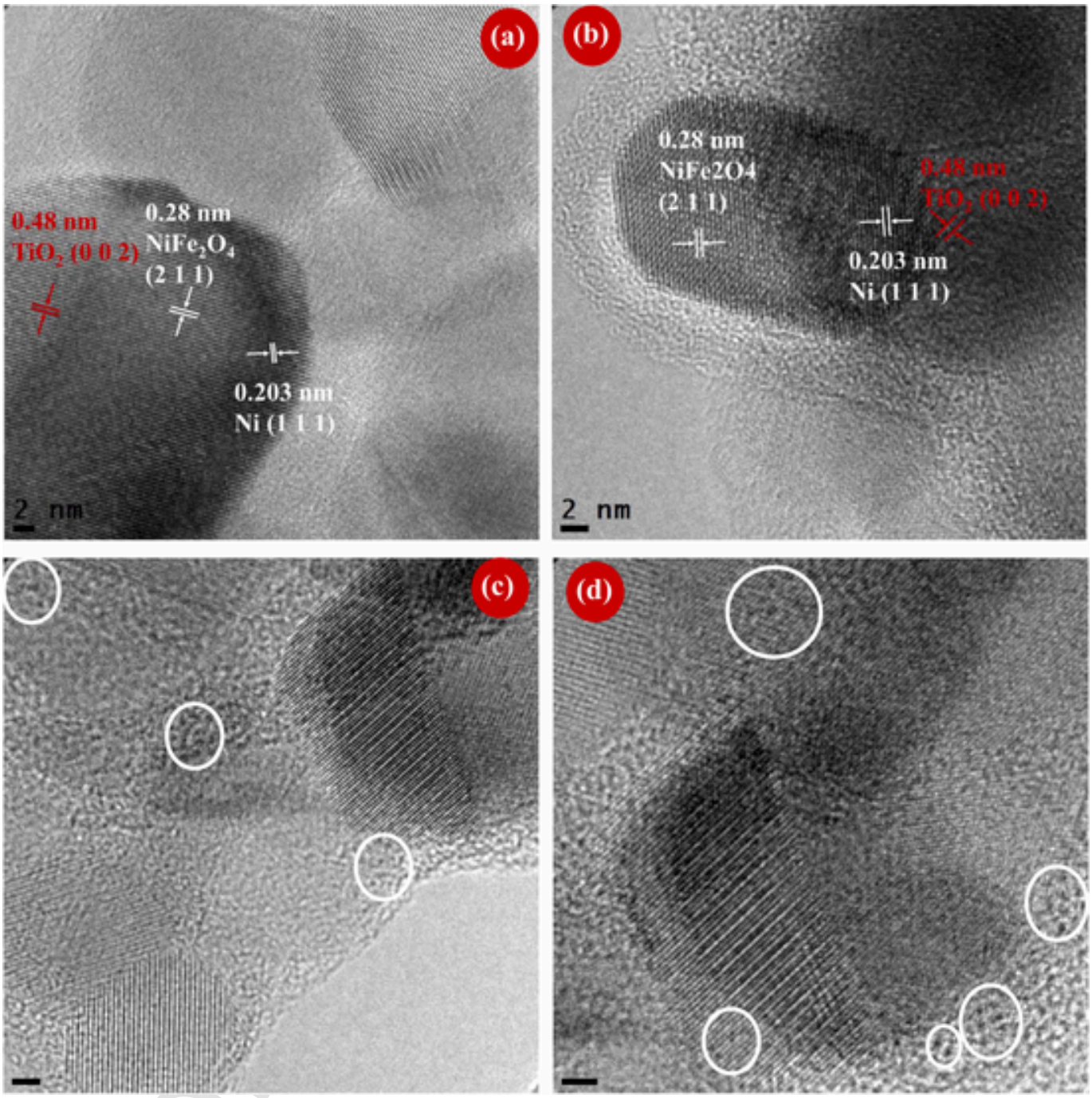

Fig. 2. High resolution TEM micrographs of Ni@$NiFe_2O_4$/TiO_2 magnetic nanocomposites. Circled portions indicate the presence of ultra-small nickel nanoparticles at $NiFe_2O_4$/TiO_2 magnetic nanocomposites.

also supported by the high-resolution TEM analysis (Fig. 2). The crystal planes corresponding to α-Fe_2O_3 (JCPDS file no. 39–1346) was detected as secondary phase during the preparation of Ni@$NiFe_2O_4$/TiO_2 magnetic nanocomposites. However, no diffractions of NiO crystal planes were detected in XRD. The diminutive formation of Fe_2O_3 along with the magnetic nanocomposites can be accounted by the migration of Fe^{3+} ions into TiO_2 lattice structure which is more favorable during the high-temperature treatment [17,22,30,42].

The appearance of Raman phonon at ~ 540 cm^{-1} designates the formation of nickel nanoparticles at the surface of $NiFe_2O_4$ magnetic nanoferrites during the Raman spectral analysis (Fig. 5A). Thus, further evidenced the formation of ultra-small nickel nanoparticles at the surface of NiO_x layer which is in good agreement with the reported Raman phonons for nickel nanoparticles [12,49,50]. The Raman bands observed at 267, 335, 483, 571 and 697 cm^{-1} indicate 3 F_{2g}, E_g and A_{1g} phonon modes of $NiFe_2O_4$ spinel ferrite crystal structure. The detected Raman phonons consistent to nickel metal nanoparticles and spinel ferrites confirms the formation of Ni@$NiFe_2O_4$ (Fig. 5A). Bare TiO_2 shows E_g, B_{1g} and A_{1g} Raman phonons at 638, 519 and 399 cm^{-1} (Fig. 5B) corresponding to the pristine crystal structure [9]. Ni@$NiFe_2O_4$/TiO_2 exhibits Raman phonon modes of nickel nanoparticles (~ 540 cm^{-1}), spinel crystal structure of $NiFe_2O_4$ and TiO_2 pristine crystal structure (Fig. 5B). The Raman spectral analysis additionally confirmed the formation of Ni@$NiFe_2O_4$/TiO_2 magnetic nanocomposites were resulted from the synthetic approach. Moreover, the intensity of Ni@$NiFe_2O_4$

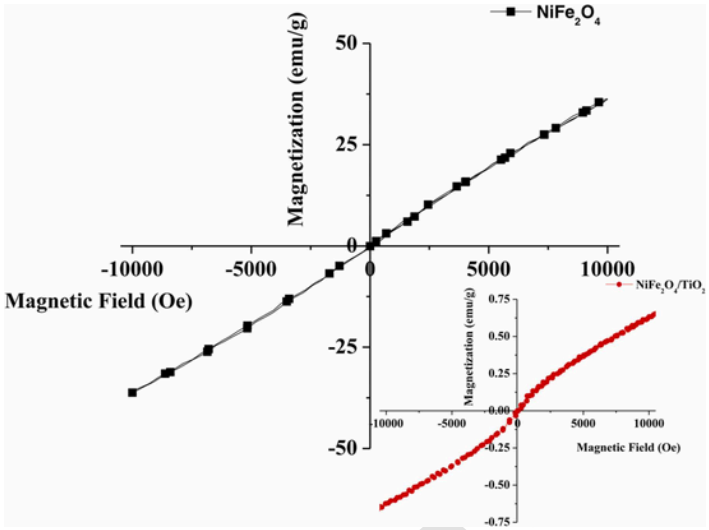

Fig. 3. Magnetic-hysteresis (M-H) loop recorded at room temperature for $NiFe_2O_4$ magnetic nanoferrites during VSM analysis. Insert shows the M-H loop recorded for $Ni@NiFe_2O_4/TiO_2$ magnetic nanocomposites.

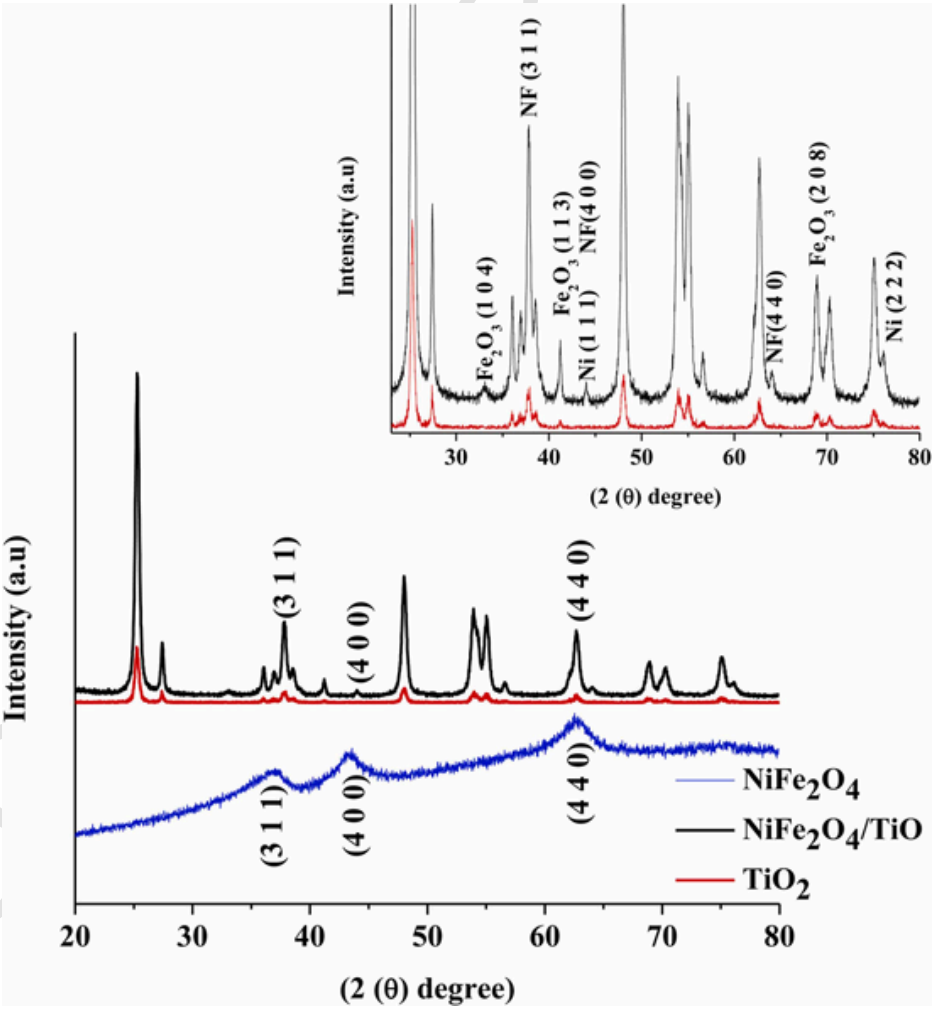

Fig. 4. X-ray diffraction (XRD) pattern of various nanocatalysts and the insert demonstrates magnified XRD of magnetic nanocomposites. Crystal planes marked in the insert indicates Ni – nickel nanoparticles; Fe_2O_3 – Hematite and NF – $NiFe_2O_4$ magnetic nanoferrites.

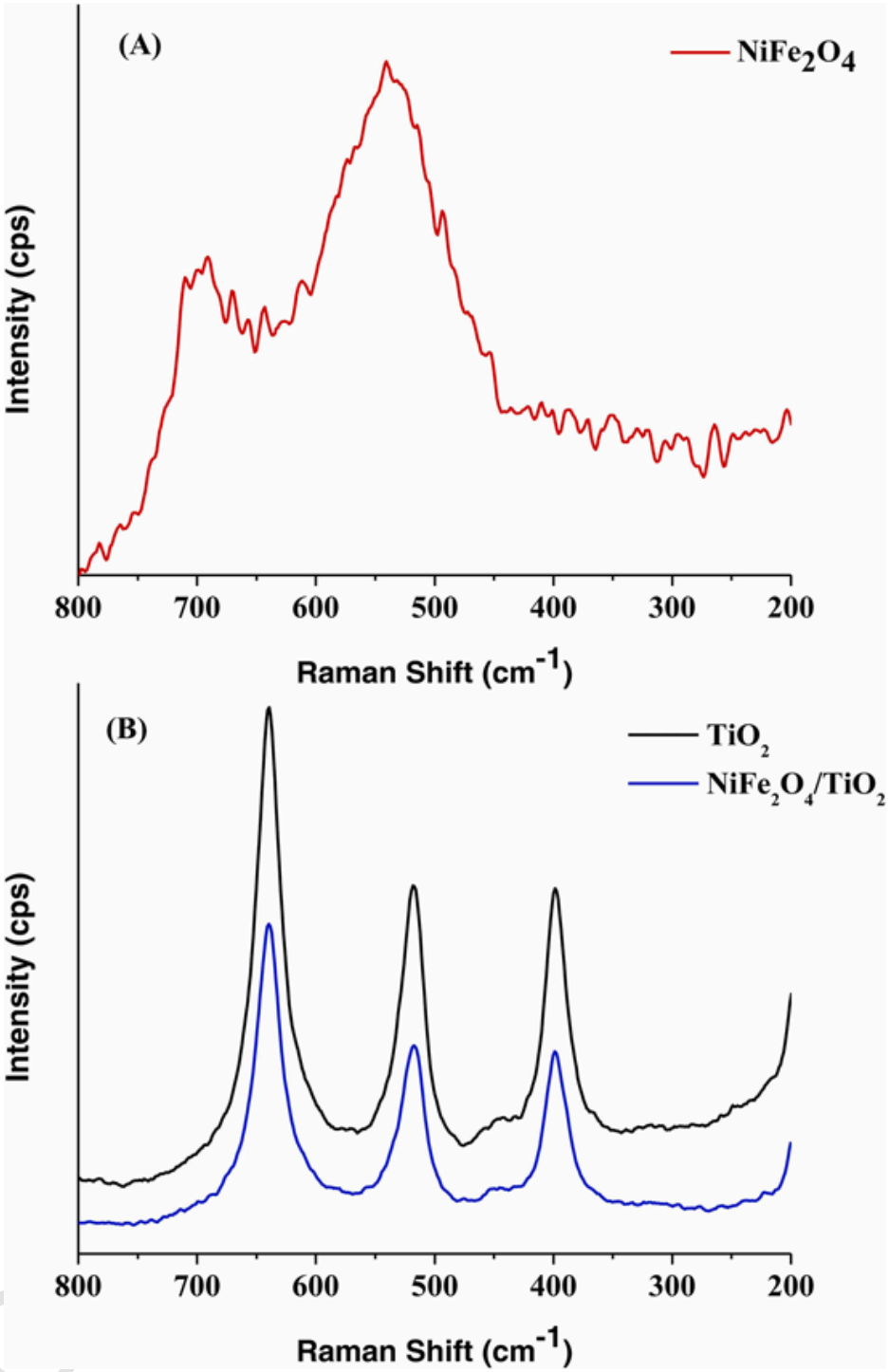

Fig. 5. Raman spectrum of Ni@$NiFe_2O_4$ magnetic nanoferrites (A) and (B) corresponds to Raman spectrum of Ni@$NiFe_2O_4$/TiO_2 magnetic nanocomposites.

Raman phonons was decreased when compared to bare TiO_2 because of the surface covering of TiO_2 over Ni@$NiFe_2O_4$ (Fig. 5B).

The diffuse reflectance (DR) UV–vis analysis of bare TiO_2 shows the absorption band edge of ~ 390 nm and TiO_2 cannot be able to produce the electronic charge carriers (e^- and h^+) in the presence of the visible light irradiation (Fig. 6 A). Besides, Ni@$NiFe_2O_4$ and Ni@$NiFe_2O_4$/TiO_2 displays the broad absorption in the DR-UV-Vis spectral analysis and the absorption decreased near infrared region (Fig. 6 A), which significantly notates the as-prepared magnetic nanocomposites will be able to generate electronic charge carriers (e^- and h^+) production with low-energy irradiation. The absorption bands at 330 – 350 and 505 – 545 nm confirm surface plasmon resonance (SPR) of nickel nanoparticles, which authorize the formation of nickel metal nanoparticles at the Ni@$NiFe_2O_4$ and Ni@$NiFe_2O_4$/TiO_2 magnetic nanocomposites [24–27,30,39,51,52]. The absorption band ranging from 650 to 750 nm observed in the as-prepared magnetic nanocomposites demonstrated the presence of oxides of Ni^{2+} and Fe^{3+} cations [17,25,26,28,30,36,37]. Moreover, the absorption band edge of Ni@$NiFe_2O_4$/TiO_2 magnetic nanocomposite was redshifted (~550 nm) when compared to bare TiO_2. Therefore, as-prepared magnetic nanocomposites can be excited with low-energy irradiation. The optical bandgap of the magnetic nanocomposites was derived from DR-UV–vis spectral analysis using

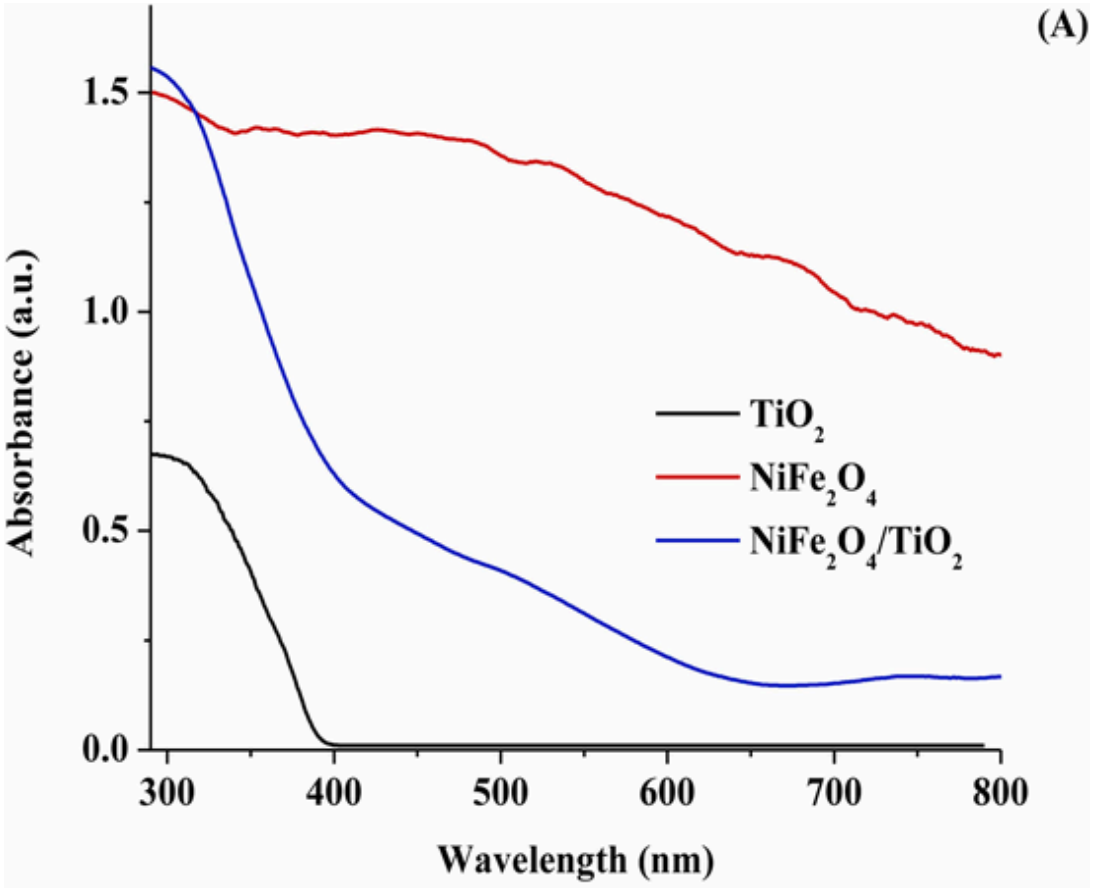
(A)
Absorbance (a.u.)
Wavelength (nm)
TiO2
NiFe2O4
NiFe2O4/TiO2

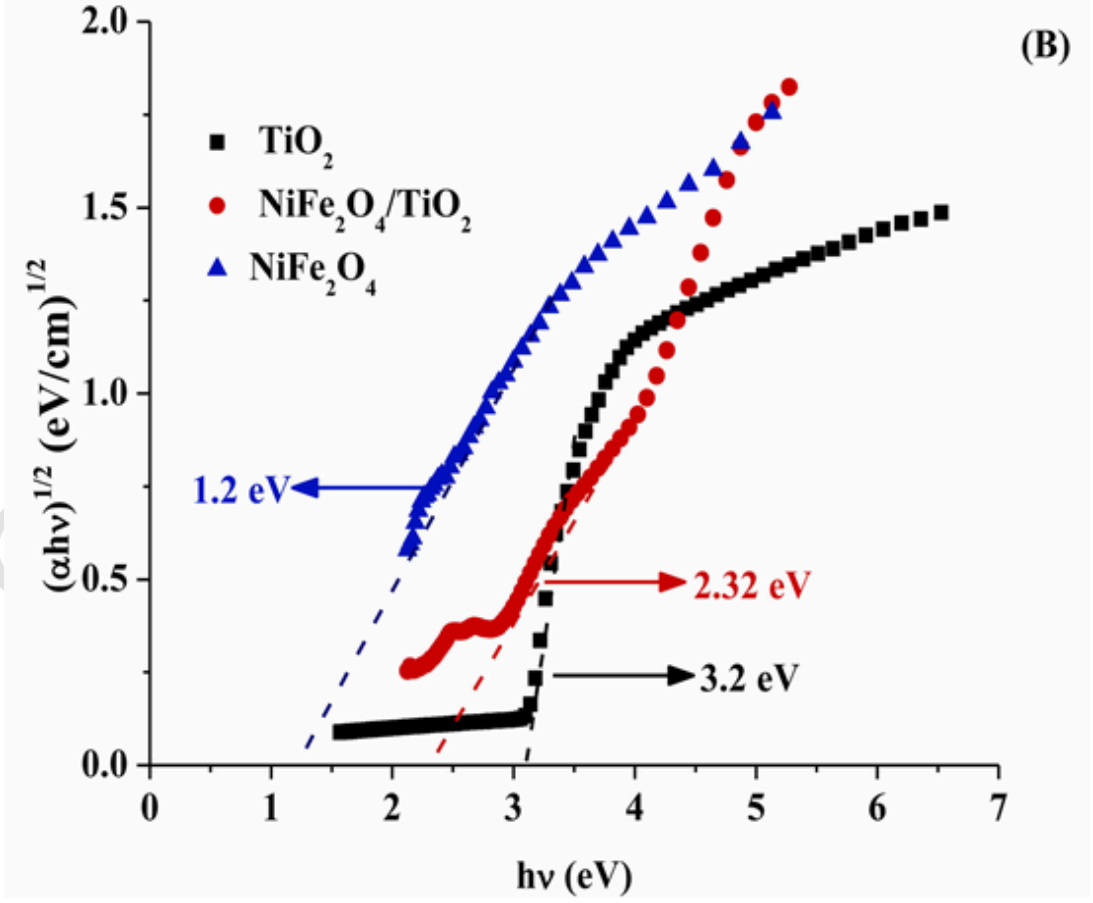
(B)
(αhν)1/2 (eV/cm)1/2
hν (eV)
TiO2
NiFe2O4/TiO2
NiFe2O4
1.2 eV
2.32 eV
3.2 eV

Fig. 6. (A) Diffuse reflectance UV-Vis spectrum of various nanocatalysts and (B) corresponding Tauc plot derived from diffuse reflectance UV-Vis spectra for various nanocatalysts.

Tauc's approach (Fig. 6B). Bare TiO_2 shows 3.2 eV whereas Ni@$NiFe_2O_4$ and Ni@$NiFe_2O_4$/TiO_2 reveal 1.2 and 2.32 eV optical bandgap, respectively.

3.2. Evaluation of photocatalytic efficiency

The solar light-driven photocatalytic efficiency of various nanocatalysts was evaluated by monitoring the simazine degradation (SZN) which is selected as the target pollutant. The maximum solubility of simazine was fixed as the initial concentration (6.2 mg/L (at 40 °C)) for the solar light-driven photocatalytic degradation. The influence of different catalyst dosage was assessed towards the degradation of SZN. The concentration of $NiFe_2O_4$/TiO_2 was set at 0.1–0.5 g/L and the observed results are given in the Fig. S1. The rate constant for SZN degradation is increased from 3×10^{-4} s^{-1} to 12.5×10^{-4} s^{-1} with respective of 0.1–0.5 g/L catalyst was added. High catalyst dosage was beneficial to improve SZN degradation efficiency, which could give more active species and active sites. However, the observed results indicate that rate constant of SZN degradation is increased from 3×10^{-4} s^{-1} to 11×10^{-4} s^{-1} when the catalyst dosage from 0.1 to 0.3 g/L. Besides, catalyst dosage increased beyond 0.3 g/L, a slight increment in the degradation is observed. In order to save costs, this study chose to add 0.3 g/L of catalyst for further studies. The kinetics of degradation was followed in the presence of various nanocatalysts. The control photocatalytic experiments (Fig. 7a) indicate that simazine degradation cannot be initiated in the presence of solar light alone (photolysis). The concentration of simazine was transformed with respect to the time progress of degradation {-ln $(SZN)_t/(SZN)_0$ vs Time} (Fig. 7a), it resulted a linear change in $[(SZN)_t/(SZN)_0]$ along with the presence of nanocatalysts, which can be corroborated to the pseudo first order kinetic degradation of simazine. $NiFe_2O_4$/TiO_2 demonstrated the maximum degradation of simazine when compared to $NiFe_2O_4$ and TiO_2 counterparts of the magnetic nanocomposites at the present experimental conditions (Fig. 7a).

The representative 3-dimentional HPLC chromatogram (3-D HPLC) of photocatalytic degradation of simazine in the presence of $NiFe_2O_4$/TiO_2 magnetic nanocomposites is shown in Fig. 7b. It designates that the simazine can be degraded in 60 min of solar light irradiation in the presence of $NiFe_2O_4$/TiO_2 magnetic nanocomposites. The initial solution clearly establishes the existence of Simazine (6-chloro-N,N′-diethyl-1,3,5-triazine-2,4-diamine) at (retention time (RT) = 4.0 min), indicated that purity of the solution. The disappearance of a strong intensified peak (retention time (RT) = 4.0 min) after 30 min of photocatalysis specifies the degradation of simazine, at the same time Fig. 7b signifies the formation of byproducts of simazine (RT = 2–3.5 min). The fastest elution of byproducts was noticed when compared to the simazine, which indicates that the daughter compounds are more polar than the parent compound. This could be the hydroxylated derivatives of Simazines, which are the major intermediates (1,1′-[(6-chloro-1,3,5-triazine-2,4-diyl)diimino]diethanol (m/z = 234) and 4,6-bis(ethylamino)– 1,3,5-triazin-2-ol (m/z = 184)[40]. In addition, the peak at RT = 2 min split into two and reduce the peak intensity of 3.5 min at after 40 min solar photocatalytic irradiation. This might be hydroxylated Simazine might be produce 6-chloro-1,3,5-triazine-2,4-diamine and N-(4-amino-6-hydroxy-1,3,5-triazin-2-yl)acetamide as the intermediates and thus confirm the progress of further mineralization of Simazine. Further, the 3-D HPLC chromatogram further reveals that intensity of byproducts decreased pertaining to progress of $NiFe_2O_4$/TiO_2 magnetic nanocomposites assisted solar light-driven photocatalysis. As evidenced from Fig. 7b approximately 90% of simazine and its byproducts were degraded within 60 min of solar light-driven photocatalysis. Based on our observed results, we anticipate that the proposed Simazine degradation pathway will exhibit similarities to pathways reported in existing studies [40,41].

In order to increase the degradation of simazine, electron acceptor peroxymonosulphate (PMS; commercially known as Oxone) was added to the photocatalytic microenvironment at the optimized conditions ($[NiFe_2O_4/TiO_2]$ = 0.3 g/L; [SZN] = 6.2 mg/L). PMS will not be able to produce any radicals when it undergoes the photolysis reaction since it requires the electrons for the activation [32,37,39,42]. The impact of different PMS concentration (0.1–0.6 mM) on SZN degradation efficiency was assessed and its results are given in the Fig. S2**.** The concentration of PMS was increased from 0.1 to 0.4 mM and the rate constant for SZN degradation in 30 min was significantly improved with linearly. However, when 0.5 mM and 0.6 mM PMS were added, the rate constant for SZN degradation was not significantly improved. This indi-

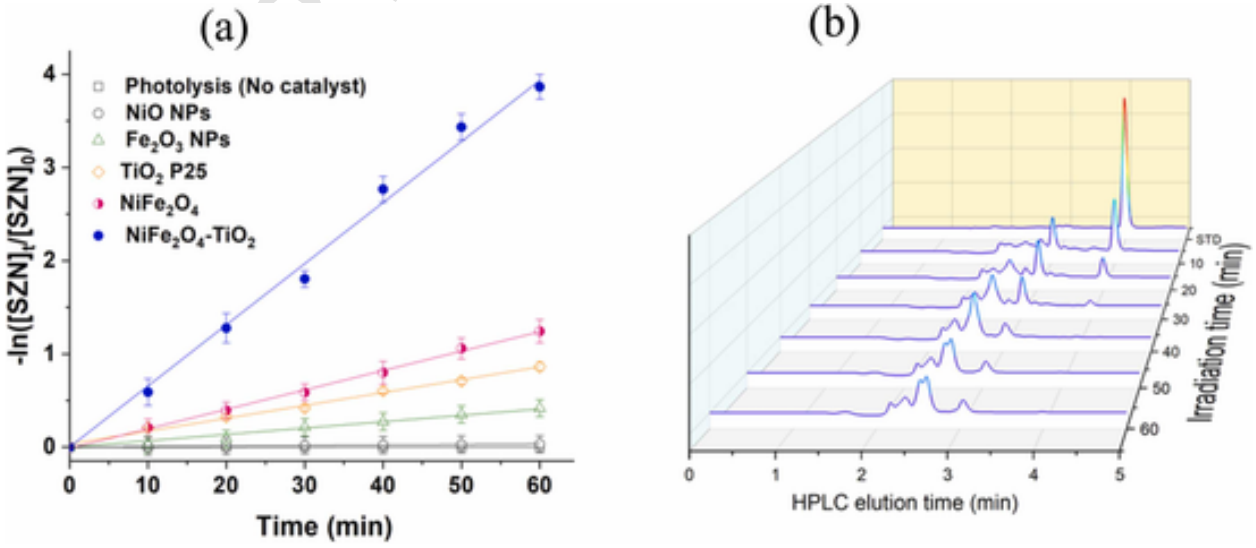

Fig. 7. (a) Plot of $-\ln([SZN]_t/[SZN]_0)$ for various nanophotocatayst employed to study the kinetic degradation of simazine; {SZN - simazine}. (b) 3-D plot demonstrating evolution of HPLC chromatogram of photocatalytic degradation of simazine. Experimental parameter: $[NiFe_2O_4/TiO_2]$ = 0.3 g/L; [SZN] = 6.2 mg/L, [T] = 25 °C.

cated that $SO_4^{\bullet-}$ would spontaneously react when the concentration of PMS and catalyst reached equilibrium [32,37,39,42] (Eqs. (2) and (3)).

$$HSO_5^- + SO_4^{\bullet-} \rightarrow SO_5^{\bullet-} + SO_4^{2-} + H^+ \quad (2)$$

$$SO_4^{\bullet-} + SO_4^{\bullet-} \rightarrow S_2O_8^{2-} \quad (3)$$

At the optimized photocatalytic degradation condition of simazine, PMS [0.4 mM] was added and the subsequent kinetics of photocatalytic degradation was followed by the HPLC analysis. Fig. 8a shows that the HPLC peak corresponding to simazine (RT = 4.0 min) was completely disappeared in 12 min which indicates that the kinetics of degradation was achieved faster rate in the $NiFe_2O_4/TiO_2$ + PMS system. PMS will tends to produce the sulphate ($SO_4^{\bullet-}$) and hydroxyl (•OH) radicals in addition to the hydroxyl radical generated during photocatalysis [5,24, 31–33,39,42]. The augmentation of radicals in the photocatalytic microenvironment leads to degrade the simazine faster when compared to the absence of PMS. Further the new peaks were originated (RT = 2–3 min) after 10 min of photocatalytic degradation of simazine (Fig. 8a) in the presence of PMS indicates the formation of various intermediates. However, simazine and its intermediates were degraded as on progress of the photocatalytic degradation. The degradation of simazine in the presence of PMS and various nanocatalysts is portrayed in Fig. 8b. It can be inferred from Fig. 8b that no significant degradation rate of simazine can be observed during the photolysis + PMS; NiO + PMS when compared to the maximum efficiency achieved during the solar light-driven photocatalysis in the presence of $NiFe_2O_4/TiO_2$ along with the presence of PMS. In addition, *3-fold* enhanced degradation rate is observed for the $NiFe_2O_4/TiO_2$ + PMS when compared to $NiFe_2O_4/TiO_2$ magnetic nanocomposites alone. The kinetic rate attained for the simazine degradation in the presence of PMS and the counterparts of $NiFe_2O_4/TiO_2$ magnetic nanocomposites is shown in Fig. 8b to comprehend the role of $NiFe_2O_4/TiO_2$ + PMS since the 0.4 mM of PMS with other nanocatalysts cannot be efficient (Fig. 9a).

The rate constant (k′) observed for the degradation of simazine in the presence of various nanocatalysts and PMS is shown in Fig. 9a. The k′ resulted from the simazine degradation for the photolysis, photolysis + PMS and NiO can be negligible when compared to the k′ observed for the other photocatalytic degradation systems. Fe_2O_3, TiO_2 (P25) and $NiFe_2O_4$ nanocatalysts exhibited efficient degradation when compared to their counterparts. Whereas if the PMS is added to the photocatalytic microenvironment the rate of simazine degradation was almost doubled for the Fe_2O_3, TiO_2(P25) and $NiFe_2O_4$ nanocatalysts which indicates the degradation of simazine proceeded faster when compared to the bare photocatalytic systems. Fig. 9b demonstrates the removal percentage of simazine, 99.2% efficient removal was observed for the $NiFe_2O_4$/PMS and $NiFe_2O_4/TiO_2$ mediated photocatalytic degradation when the slurry was irradiated for 40 min whereas $NiFe_2O_4/TiO_2$ with PMS degraded the simazine within 20 min of the solar light irradiation.

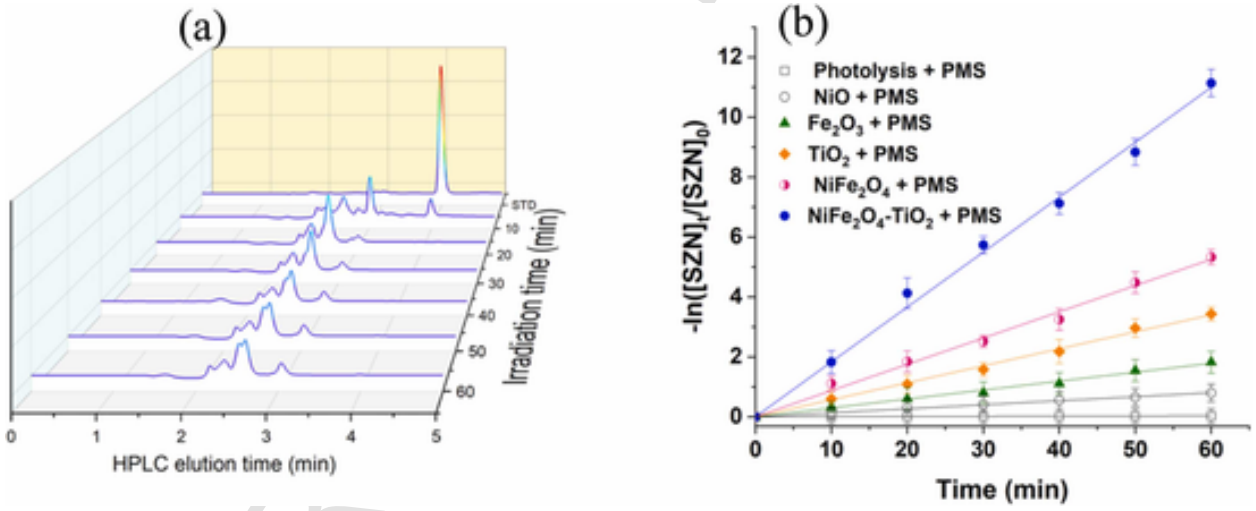

Fig. 8. (a) Plot of –ln([SZN]$_t$/[SZN]$_0$) for various nanophotocatayst employed to study the kinetic degradation of simazine in the presence of PMS {peroxymonosulphate; SZN - simazine}. (b) 3-D plot demonstrating evolution of HPLC chromatogram of photocatalytic degradation of simazine. Experimental parameter: [Catalyst] = 0.3 g/L; [SZN] = 6.2 mg/L, [PMS] = 0.4 mM; [T] = 25 °C.

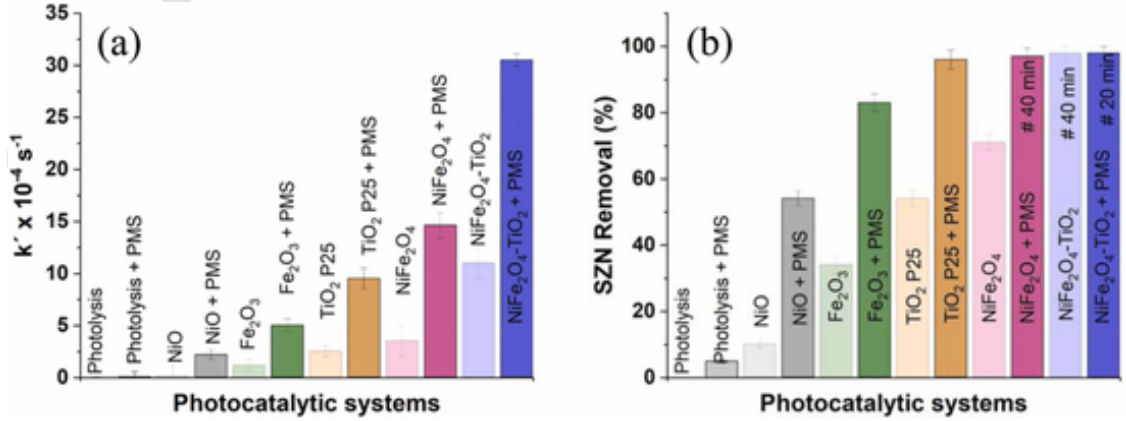

Fig. 9. Comparison of apparent rate constants observed for the degradation of simazine in presence of various nanocatalysts and PMS employed at its optimized Experimental parameter: [Catalyst] = 0.3 g/L; [SZN] = 6.2 mg/L, [PMS] = 0.4 mM; [T] = 25 °C.

A *2-fold* enhanced rate of degradation could be achieved for the degradation of simazine. It is also noticed from Fig. 9b that the bare nanocatalysts with and without combination of PMS revealed relatively low efficiency for the removal of simazine even after 60 min of the solar light irradiation.

The initial pH of the solution exerted a distinct influence on both the catalytic surface charge performance and production of free radicals within the system. In this context, the influence of different initial pH of the solution was assessed towards the degradation of SZN at optimized conditions ([$NiFe_2O_4/TiO_2$] = 0.3 g/L; [SZN] = 6.2 mg/L; [PMS] = 0.4 mM) and the observed results are given in the Fig. S3. As illustrated in Fig. S3, as the pH increased from 3.0 to 7.0 the degradation of SZN increased significantly. Whereas, degradation of SZN decreased with further increasing of pH to 11. The experimental results exhibits that the presence of H^+ ions at lower pH could be quenched the $SO_4^{\bullet-}$ and •OH (Eqs. (4) to (6)). Besides, at higher pH value, the rate of SZN degradation is reduced. This may be because excessive OH^- radicals scavenged $SO_4^{\bullet-}$ to generate •OH radicals (Eq. (5)), which have a lower oxidation capacity than $SO_4^{\bullet-}$. As consequence, reduction of oxidative radical in the solution bulk leaded to the reduction of SZN degradation efficiency. The current results are consistent with the previously reported research results on the PMS activation over nanocatalysts [53–57].

$$SO_4^{\bullet-} + H^+ \quad e^- \rightarrow HSO_4^- \tag{4}$$

$$HO^{\bullet} + H^+ + e^- \rightarrow H_2O \tag{5}$$

$$SO_4^{\bullet-} + HO^- \left(H_2O\right) \rightarrow SO_4^{2-} + HO^{\bullet}(+H^+) \tag{6}$$

In actual wastewater, there exist different kinds of inorganic anions and organic matters, influencing the performance of the catalyst/oxidant towards degradation of the SZN. The effects of different coexisting anions (HCO_3^-, Cl^-, NO_3^-, HPO_4^{2-}) and organic matter (Humic acid) on SZN degradation are shown in Fig. S4. The observed results at optimized conditions ([$NiFe_2O_4/TiO_2$] = 0.3 g/L; [SZN] = 6.2 mg/L; [PMS] = 0.4 mM; [foreign substance] = 0.1 g/L) exhibits that the foreign substance such as HCO_3^-, Cl^-, NO_3^-, HPO_4^{2-} and humic acid are affect the rate constant of SZN degradation. This could be quenching of oxidative radical ($SO_4^{\bullet-}$ and •OH) (Eqs. (7)–(12)) leads to formation of minimum quantity species hindered the degradation of SZN. This inhibitory effect was HPO_4^{2-} > HA > HCO_3^- > NO_3^- > Cl^- and the observed results are harmony with the previous results [53–57] In addition, to determine the applicability of the $NiFe_2O_4/TiO_2$ + PMS system in actual water matrix, four typical surface water sources, i.e., Milli-Q water, municipal tap water, groundwater and wastewater were used as water matrixes for degradation process. The physiochemical properties of the water samples are listed in Table S1. The experimental findings presented in Fig. S5 reveal that the rate constants of SZN degradation exhibited slight to moderately inhibitory effects. These effects were attributed to the relatively higher concentration of dissolved organics, coexisting anions, as well as total dissolved solids (TDS) and turbidity. Collectively, these constituents introduced adverse impacts on the degradation of SZN. They did so by scavenging reactive radicals, buffering pH, scattering incident radiation, and obstructing the catalyst pores, thereby impeding the transport of reactive species to the active sites. Quantitatively, milli-Q water, SZN degradation reached an impressive 100%, while in tap water, groundwater, and wastewater, the degradation were notably lower at 82.2%, 64.1%, and 50.8%, respectively, under 60 min direct solar light irradiation at optimized experimental conditions ([$NiFe_2O_4/TiO_2$] = 0.3 g/L; [SZN] = 6.2 mg/L; [PMS] = 0.4 mM).

$$SO_4^{\bullet-} + Cl^- \rightarrow Cl^{\bullet} + SO_4^{2-} \tag{7}$$

$$Cl^{\bullet} + Cl^- \rightarrow Cl^{2-} \tag{8}$$

$$Cl^- + HO^{\bullet} \rightarrow ClOH^- \tag{9}$$

$$ClOH^- + H^+ \rightarrow H_2O + Cl^{\bullet} \tag{10}$$

$$CO_3^{2-} + SO_4^{2-} \rightarrow SO_4^{2-} + CO_3^{\bullet-} \tag{11}$$

$$CO_3^{2-} + HO^{\bullet} \rightarrow HO^- + CO_3^{\bullet-} \tag{12}$$

Photoluminescence analysis of the $NiFe_2O_4/TiO_2$/PMS system involved the use of terephthalic acid (TA) aqueous solution traps to gain insights into the active species participating in the reaction. Notably, when the TA aqueous solution was examined, it displayed no observable photoluminescence (FL) intensity at a peak wavelength of 425 nm. This absence of FL intensity was observed both in the presence of the catalyst under dark conditions and during irradiation in the absence of the porous $NiFe_2O_4/TiO_2$/PMS system, as shown in Fig. S6. However, a significant FL intensity was observed when the terephthalic acid aqueous solution was irradiated directly with solar light in the presence of either $NiFe_2O_4/TiO_2$ or $NiFe_2O_4/TiO_2$/PMS systems. This observation suggests that photocatalytic reactions generate hydroxyl radicals (•OH), which, when they react with TA, lead to the formation of the fluorescent 2-hydroxyterephthalic acid (HTA). The calculated production of •OH radicals after one hour of irradiation indicates that the concentration of •OH radicals is higher in the assessed photocatalyst systems, namely $NiFe_2O_4/TiO_2$ (9.10×10^{-6} M) and $NiFe_2O_4/TiO_2$/PMS (1.28×10^{-5} M). These findings align with the observed efficiencies in SZN degradation for $NiFe_2O_4/TiO_2$ and $NiFe_2O_4/TiO_2$/PMS, as shown in Figs. 7a and 8b. In order to gain a deeper understanding of the contribution of the oxidative radicals to the degradation process, oxidative radical species trapping experiments were conducted within the $NiFe_2O_4/TiO_2$ and $NiFe_2O_4/TiO_2$/PMS system (as shown in Table S2). Tert-butanol (TBA), known as a scavenger for •OH radicals, was introduced during the degradation of SZN under optimized conditions ([$NiFe_2O_4/TiO_2$] = 0.3 g/L; [SZN] = 6.2 mg/L; [PMS] = 0.4 mM; [TBA] = 0.3 M). The results of these experiments demonstrated that when the presence of TBA, the degradation efficiency of SZN decreased significantly, reaching approximately 99% reduction for $NiFe_2O_4/TiO_2$ and 35% reduction for $NiFe_2O_4/TiO_2$/PMS system. This inhibitory effect strongly supports the conclusion that $SO_4^{\bullet-}$ radicals play a major role in the degradation of SZN in the presence of the $NiFe_2O_4/TiO_2$/PMS.

The introduction of narrow-band-gap semiconductor ($NiFe_2O_4$ = 1.2 eV) into wide-band-gap semiconductor TiO_2 = 3.2 eV by the formation of heterojunction provides a new internal band energy level $NiFe_2O_4/TiO_2$ = 2.32 eV between the conduction and valence bands of TiO_2. This newly formed internal energy level plays a crucial role in promoting the migration of electrons and holes in different directions in response to the energy of incident light. During the photocatalytic process, electrons from the valence band of $NiFe_2O_4/TiO_2$ get excited to this new energy level within the conduction band of $NiFe_2O_4/TiO_2$. Consequently, the photogenerated electrons and holes disperse over the surface of $NiFe_2O_4$. The photogenerated electrons efficiently interact with dissolved oxygen to generate $^{-\bullet}O_2$ radicals, which further lead to the formation of •OH radicals. In the presence of PMS, the photogenerated electrons also react with PMS molecules, resulting in the generation of $SO_4^{\bullet-}$ radicals and •OH radicals. This separation and efficient utilization of photogenerated electron-hole pairs reduce the recombination accordingly, thereby enhancing the overall photocatalytic oxidation of SZN. In summary, these formed radicals significantly contribute to the increased efficacy of the photocatalytic degradation of SZN.

The total organic carbon (TOC) removal for the simazine degradation was analyzed for 6 h of solar light irradiation at the optimized condition {simazine 6.2 mg/L; [nanocatalyst] = 0.3 g/L and [PMS] = 0.4 mM}. The photolysis with and without the combination of PMS showed a negligible amount of mineralization when compared to other photocatalytic systems (Fig. 10) whereas the bare nanocatalysts (NiO, Fe_2O_3, TiO_2 and $NiFe_2O_4$) exhibited 25–60% of mineralization of simazine respectively in the present experimental conditions. On the other hand, the bare nanocatalysts with the combination of PMS

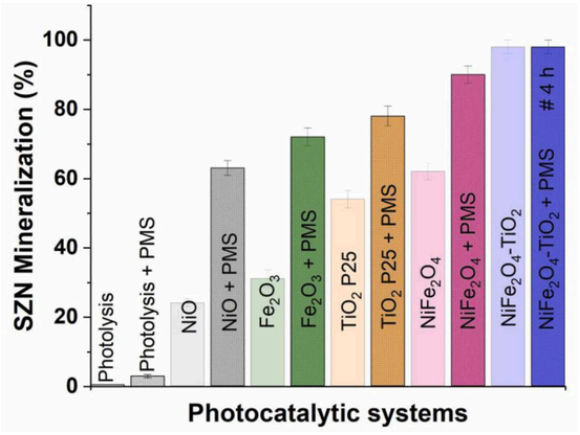

Fig. 10. Total organic carbon (TOC) removal in percentage of simazine. Experimental parameter: [Catalyst] = 0.3 g/L; [SZN] = 6.2 mg/L, [PMS] = 0.4 mM; [T] = 25 °C.

demonstrated the mineralization of simazine from 63% to 90%. Simazine mineralization efficacy was achieved 100% for 6 h irradiation in the presence of $NiFe_2O_4/TiO_2$ magnetic nanocomposites whereas in combination with PMS 100% mineralization was resulted for 4 h of solar light irradiation. The addition of PMS to the photocatalytic microenvironment certainly enhances the hydroxyl (•OH) and sulphate (SO_4•−) radicals in addition to the hydroxyl (•OH) radicals generated from the solar light-driven photocatalysis [5,24,31–33,39,42]. Consequently, enhanced mineralization was resulted in the combination of $NiFe_2O_4/TiO_2$ with PMS.

In order to check the stability of the $NiFe_2O_4/TiO_2$ magnetic nanocomposites, the nanocatalysts were collected after the completion of photocatalytic degradation experiments and washed with distilled water under vigorous stirring for three times subsequently dried at room temperature for further recycling. The as-prepared $NiFe_2O_4/TiO_2$ magnetic nanocatalysts were more stable and the efficiency of Simazine degradation was approximately same for the continuous five cycles (Fig. 11) at the optimized experimental conditions. After the fifth cycle the efficacy of the synthesized $NiFe_2O_4/TiO_2$ magnetic nanocomposites was found to decline the efficiency.

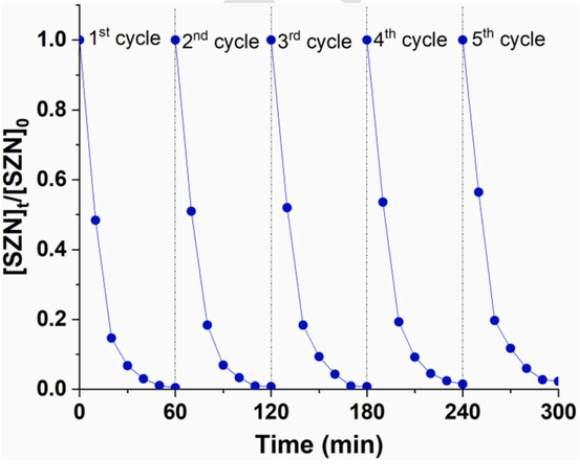

Fig. 11. Stability study of the $NiFe_2O_4/TiO_2$ nanocatalysts was conducted without the addition of PMS. Operating conditions: [SZN] = 6.2 mg/L; [catalyst] = 0.3 g/L.

4. Conclusion

In summary, ultra-small Ni nanoparticles modified $Ni@NiFe_2O_4/TiO_2$ magnetic nanocomposites were successfully synthesized and applied to activate PMS by the photocatalytic process to generate hydroxyl (•OH) and sulphate (SO_4•−) for simazine oxidation under the natural solar light irradiation. $Ni@NiFe_2O_4/TiO_2$ exhibited high efficient catalytic performance towards the oxidation of simazine. The photocatalytic oxidation efficiency of $Ni@NiFe_2O_4/TiO_2$ against simazine 6.2 (mg/L) could reach 99% within 60 min, which is significantly higher and faster than those of commercial TiO_2 NPs. These high photocatalytic properties attributed to the effective formation of a heterojunction between ultra-small Ni NPs modified magnetic $Ni@NiFe_2O_4$ and non-magnetic TiO_2 NPs. In addition, $Ni@NiFe_2O_4/TiO_2$ + PMS system exhibited 3 and 7-folds higher the catalytic activity compared to $Ni@NiFe_2O_4/TiO_2$ and the commercial TiO_2 NPs, respectively. Besides, the TOC removal experiments, clearly showed that 99% simazine could mineralized into CO_2 and H_2O within 4 h in the presence of $Ni@NiFe_2O_4/TiO_2$ + PMS system under the natural solar light irradiation which further showed its effectiveness in the pollutant removal. The reusability study confirmed that the synthesized nanocatalyst was stable with no change in its efficiency until the five consecutive cycles. Overall, these findings provided a novel photocatalyst with an effective visible light response and reusability that could be applied as a new photocatalytic process assisted by PMS activation in the large-scale wastewater treatment facilities.

CRediT authorship contribution statement

C. Ashina: Methodology, Investigation, Formal analysis, Visualization, Validation. **N. Pugazhenthiran**: Conceptualization, Methodology, Data curation, Formal analysis, Writing – original draft, Software, Editing, Validation. **P. Sathishkumar**: Conceptualization, Methodology, Formal analysis, Investigation, Data curation, Writing – review & editing, Supervision, Project administration, Funding acquisition. **C. Rajasekaran**: Formal analysis, Visualization, Validation. **M.A. Gracia-Pinilla**: Formal analysis, Visualization, Validation. **R.V. Mangalaraja**: Formal analysis, Visualization, Validation.

Declaration of Competing Interest

The authors declare that they have no known competing financial interests or personal relationships that could have appeared to influence the work reported in this paper.

Data availability

Data will be made available on request.

Acknowledgements

The author P. Sathishkumar thank VIT, India for providing 'VIT SEED GRANT' File No.: SG20210261 for carrying out this research work. The author N. Pugazhenthiran gratefully acknowledges ANID-FONDECYT, Santiago, Chile for Initiation grant No. 11190600 for financial support. The authors extend their appreciation to the Deanship of Scientific Research at King Khalid University for the support through the Large Research Group project under grant number, R.G.P. 2/354/44.

Data availability

Data will be made available on request.

Appendix A. Supporting information

Supplementary data associated with this article can be found in the online version at doi:10.1016/j.jece.2023.111342.

References

[1] U. Farooq, T. Ahmad, F. Naaz, Su Islam, Review on metals and metal oxides in sustainable energy production: progress and perspectives, Energy Fuels 37 (2023) 1577–1632.

[2] I. Ahmad, Y. Zou, J. Yan, Y. Liu, S. Shukrullah, M.Y. Naz, H. Hussain, W.Q. Khan, N.R. Khalid, Semiconductor photocatalysts: A critical review highlighting the various strategies to boost the photocatalytic performances for diverse applications, Adv. Colloid Interface Sci. 311 (2023) 102830.

[3] A. Krishnan, A. Swarnalal, D. Das, M. Krishnan, V.S. Saji, S.M.A. Shibli, A review on transition metal oxides based photocatalysts for degradation of synthetic organic pollutants, J. Environ. Sci. (2023).

[4] S. Nazari, E. Asgari, A. Sheikhmohammadi, S.A. Mokhtari, H. Alamgholiloo, Visible-light-driven photocatalytic activity of WO3/ZIF-67 S-scheme heterojunction for upgrading degradation of oxytetracycline, J. Environ. Chem. Eng. 11 (2023) 110393.

[5] R. Rajangam, N. Pugazhenthiran, S. Krishna, R.V. Mangalaraja, H. Valdés, A. Ravikumar, P. Sathishkumar, Solar light-driven CoFe2O4/α-Ga2O3 heterojunction nanorods mediated activation of peroxymonosulfate for photocatalytic degradation of norflurazon, J. Environ. Chem. Eng. 9 (2021) 106237.

[6] Q. Guo, C. Zhou, Z. Ma, X. Yang, Fundamentals of TiO2 photocatalysis: concepts, mechanisms, and challenges, Adv. Mater. 31 (2019) 1901997.

[7] J. Schneider, M. Matsuoka, M. Takeuchi, J. Zhang, Y. Horiuchi, M. Anpo, D.W. Bahnemann, Understanding TiO2 photocatalysis: mechanisms and materials, Chem. Rev. 114 (2014) 9919–9986.

[8] X. Yang, D. Wang, Photocatalysis: from fundamental principles to materials and applications, ACS Appl. Energy Mater. 1 (2018) 6657–6693.

[9] S.A. Anjugam Vandarkuzhali, N. Pugazhenthiran, R.V. Mangalaraja, P. Sathishkumar, B. Viswanathan, S. Anandan, Ultrasmall Plasmonic Nanoparticles Decorated Hierarchical Mesoporous TiO2 as an Efficient Photocatalyst for Photocatalytic Degradation of Textile Dyes, ACS Omega 3 (2018) 9834–9845.

[10] R. Verma, R. Belgamwar, P. Chatterjee, R. Bericat-Vadell, J. Sa, V. Polshettiwar, Nickel-Laden Dendritic Plasmonic Colloidosomes of Black Gold: Forced Plasmon Mediated Photocatalytic CO_2 Hydrogenation, ACS Nano 17 (2023) 4526–4538.

[11] S. Varangane, T.P. Yendrapati, A. Tripathi, R. Thapa, S. Bojja, P. Anand, V. Perupogu, U. Pal, Integrating Ultrasmall Pd NPs into Core–Shell Imidazolate Frameworks for Photocatalytic Hydrogen and MeOH Production, Inorg. Chem. (2023).

[12] M. Singh, P. Solanki, P. Patel, A. Mondal, S. Neogi, Highly active ultrasmall Ni nanoparticle embedded inside a robust metal–organic framework: remarkably improved adsorption, selectivity, and solvent-free efficient fixation of CO2, Inorg. Chem. 58 (2019) 8100–8110.

[13] X. Bian, K. Hong, X. Ge, R. Song, L. Liu, M. Xu, Functional Hierarchical Nanocomposites Based on ZnO Nanowire and Magnetic Nanoparticle as Highly Active Recyclable Photocatalysts, The, J. Phys. Chem. C. 119 (2015) 1700–1705.

[14] A. Javaid, M. Imran, S. Latif, N. Hussain, M. Bilal, Functionalized magnetic nanostructured composites and hybrids for photocatalytic elimination of pharmaceuticals and personal care products, Sci. Total Environ. 849 (2022) 157683.

[15] R. Monsef, M. Ghiyasiyan-Arani, M. Salavati-Niasari, Design of magnetically recyclable ternary Fe2O3/EuVO4/g-C3N4 nanocomposites for photocatalytic and electrochemical hydrogen storage, ACS Appl. Energy Mater. 4 (2021) 680–695.

[16] P. Zhang, Z. Mo, L. Han, X. Zhu, B. Wang, C. Zhang, Preparation and Photocatalytic Performance of Magnetic TiO2/Montmorillonite/Fe3O4 Nanocomposites, Ind. Eng. Chem. Res. 53 (2014) 8057–8061.

[17] R. Chalasani, S. Vasudevan, Cyclodextrin-Functionalized Fe3O4@TiO2: Reusable, Magnetic Nanoparticles for Photocatalytic Degradation of Endocrine-Disrupting Chemicals in Water Supplies, ACS Nano 7 (2013) 4093–4104.

[18] S.R. Fouda, I.S. Yahia, M.S.A. Hussien, Photocatalytic degradation of methylene blue and rhodamine B using one-pot synthesized nickel oxide grafted glycine (NiO @GLY) nanostructured: Oxygen vacancies effect, J. Photochem. Photobiol. A: Chem. 439 (2023) 114622.

[19] S. Yang, S. Zhang, Q. Xu, J. Liu, C. Zhong, Z. Xie, Y. Zhao, Efficient activation of persulfate by Nickel-supported cherry core biochar composite for removal of bisphenol A, J. Environ. Manag. 324 (2022) 116305.

[20] A. Bashir, T. Munawar, F. Mukhtar, M.S. Nadeem, S. Manzoor, M.N. Ashiq, S.A. Khan, M. Koc, F. Iqbal, Dual-functional fullerene supported NiO-based nanocomposite: Efficient electrocatalyst for OER and photocatalyst for MB dye degradation, Mater. Chem. Phys. 293 (2023) 126886.

[21] M. Dib, A. Moutcine, H. Ouchetto, A. Chtaini, A. Hafid, M. Khouili, New efficient modified carbon paste electrode by Fe2O3@Ni/Al-LDH magnetic nanocomposite for the electrochemical detection of mercury, Inorg. Chem. Commun. 131 (2021) 108624.

[22] B. Sahu, U.K. Panigrahi, C.J. Sheppard, A.R.E. Prinsloo, P. Mohanty, P. Mallick, Structural and magnetic characteristics of NiO/NiFe2O4/α-Fe2O3 nanocomposite, Mater. Chem. Phys. 302 (2023) 127759.

[23] F. Mukhtar, T. Munawar, M.S. Nadeem, M. Naveed ur Rehman, S.A. Khan, M. Koc, S. Batool, M. Hasan, F. Iqbal, Dual Z-scheme core-shell PANI-CeO2-Fe2O3-NiO heterostructured nanocomposite for dyes remediation under sunlight and bacterial disinfection, Environ. Res. 215 (2022) 114140.

[24] J. Zuo, B. Wang, J. Kang, P. Yan, J. Shen, S. Wang, D. Fu, X. Zhu, T. She, S. Zhao, Z. Chen, Activation of peroxymonosulfate by nanoscaled NiFe2O4 magnetic particles for the degradation of 2,4-dichlorophenoxyacetic acid in water: Efficiency, mechanism and degradation pathways, Sep. Purif. Technol. 297 (2022) 121459.

[25] P.S.Rana Tripta, NiFe2O4/ZnO nanocomposites for degradation of MB dye with their local electrical behavior, J. Mol. Struct. 1282 (2023) 135160.

[26] P.S.Rana Tripta, Structural, optical, electrical, and photocatalytic application of NiFe2O4@NiO nanocomposites for methylene blue dye, Ceram. Int. 49 (2023) 13520–13530.

[27] T.D. Kusworo, A.C. Kumoro, N. Aryanti, H. Hasbullah, D.R.S. Chaesarifa, M.D. Fauzan, F. Dalanta, Developing a robust photocatalytic and antifouling performance of PVDF membrane using spinel NiFe2O4/GO, Photocatal. Effic. Ind. Dye Wastewater Treat., J. Environ. Chem. Eng. 11 (2023) 109449.

[28] J. Song, J. Zhang, A. Zada, Y. Ma, K. Qi, CoFe2O4/NiFe2O4 S-scheme composite for photocatalytic decomposition of antibiotic contaminants, Ceram. Int. 49 (2023) 12327–12333.

[29] Y. Li, J. Geng, Z. Wang, S. Wang, M. Wang, Boosting visible-light photocatalytic tetracycline degradation by constructing core-shell NFO@CN, Heterostruct., J. Alloy. Compd. 939 (2023) 168635.

[30] Z. Abdi, A. Malek Khachatourian, A. Nemati, Visible-light-driven photocatalytic activity of NiFe2O4@Ti-doped ZnO magnetically separable nanoparticles anchored on N-doped rGO nanosheets, Diam. Relat. Mater. 135 (2023) 109839.

[31] N. Pugazhenthiran, P. Sathishkumar, O. Albormani, S. Murugesan, M. Kandasamy, M. Selvaraj, S. Suresh, S.K. Kumar, D. Contreras, H. Váldes, R.V. Mangalaraja, Silver nanoparticles modified ZnO nanocatalysts for effective degradation of ceftiofur sodium under UV–vis light illumination, Chemosphere 313 (2023) 137515.

[32] N. Pugazhenthiran, S. Murugesan, S. Anandan, High surface area Ag-TiO2 nanotubes for solar/visible-light photocatalytic degradation of ceftiofur sodium, J. Hazard. Mater. 263 (2013) 541–549.

[33] N. Pugazhenthiran, S. Murugesan, P. Sathishkumar, S. Anandan, Photocatalytic degradation of ceftiofur sodium in the presence of gold nanoparticles loaded TiO2 under UV–visible light, Chem. Eng. J. 241 (2014) 401–409.

[34] E. Asgari, F. Mohammadi, H. Nourmoradi, A. Sheikhmohammadi, Z. Rostamifasih, B. Hashemzadeh, H. Arfaeinia, Heterogeneous catalytic degradation of nonylphenol using persulphate activated by natural pyrite: response surface methodology modelling and optimisation, Int. J. Environ. Anal. Chem. 102 (2022) 6041–6060.

[35] H. Alamgholiloo, E. Asgari, S. Nazari, A. Sheikhmohammadi, N. Noroozi Pesyan, B. Hashemzadeh, Architecture of bimetallic-MOF/silicate derived Co/NC@mSiO2 as peroxymonosulfate activator for highly efficient ciprofloxacin degradation, Sep. Purif. Technol. 300 (2022) 121911.

[36] J. Zuo, J. Shen, J. Kang, P. Yan, B. Wang, S. Wang, D. Fu, W. Wang, T. She, S. Zhao, Z. Chen, B-doped NiFe2Ox based on the activation of peroxymonosulfate for degrading 2,4-dichlorophenoxyacetic acid in water, Chem. Eng. J. (Amst., Neth.) 459 (2023) 141565.

[37] D. Wen, Z. You, K. Tian, Z. Wang, Recovery of NiFe2O4 from wastewater containing nickel citrate complexes and its application to activate peroxymonosulfate, J. Environ. Chem. Eng. 11 (2023) 109422.

[38] J. Xu, H. Olvera-Vargas, F.Y.H. Teo, O. Lefebvre, A comparison of visible-light photocatalysts for solar photoelectrocatalysis coupled to solar photoelectro-Fenton: Application to the degradation of the pesticide simazine, Chemosphere 276 (2021) 130138.

[39] M. Kohantorabi, G. Moussavi, S. Mohammadi, P. Oulego, S. Giannakis, Photocatalytic activation of peroxymonosulfate (PMS) by novel mesoporous Ag/ZnO@NiFe2O4 nanorods, inducing radical-mediated acetaminophen degradation under UVA irradiation, Chemosphere 277 (2021) 130271.

[40] P. Sathishkumar, R.V. Mangalaraja, H.D. Mansilla, M.A. Gracia-Pinilla, S. Anandan, Sonophotocatalytic (42kHz) degradation of Simazine in the presence of Au–TiO2 nanocatalysts, Applied Catalysis B: Environmental 160–161 (2014) 692–700.

[41] C. Jiang, Y. Yang, L. Zhang, D. Lu, L. Lu, X. Yang, T. Cai, Degradation of Atrazine, Simazine and Ametryn in an arable soil using thermal-activated persulfate oxidation process: Optimization, kinetics, and degradation pathway, J. Hazard. Mater. 400 (2020) 123201.

[42] K.S. Sathishkumar P, P.N. K. Guesh, R.V. Mangalaraja, K.S. Gracia-Pinilla, A. S MA, Heterogeneous sonocatalytic activation of peroxomonosulphate in the presence of CoFe2O4/TiO2 nanocatalysts for the degradation of Acid Blue 113 in an aqueous environment, J. Environ. Chem. Eng. 8 (2020) 104024.

[43] K.-i Ishibashi, A. Fujishima, T. Watanabe, K. Hashimoto, Detection of active oxidative species in TiO2 photocatalysis using the fluorescence technique, Electrochem. Commun. 2 (2000) 207–210.

[44] N. Pugazhenthiran, R.V. Mangalaraja, P. Sathishkumar, S. Murugesan, T. Muneeswaran, T. Pandiyarajan, S. Naveenraj, D. Contreras, S. Anandan, Green synthesis of porous Au–Nx-TiO2 nanospheres for solar light induced photocatalytic degradation of diazo and triazo dyes and their eco-toxic effects, N. J. Chem. 42 (2018) 18717–18728.

[45] F. Yan, D. Guo, S. Zhang, C. Li, C. Zhu, X. Zhang, Y. Chen, An ultra-small NiFe2O4 hollow particle/graphene hybrid: fabrication and electromagnetic wave absorption property, Nanoscale 10 (2018) 2697–2703.

[46] J. Liu, D. Zhu, T. Ling, A. Vasileff, S.-Z. Qiao, S-NiFe2O4 ultra-small nanoparticle built nanosheets for efficient water splitting in alkaline and neutral pH, Nano Energy 40 (2017) 264–273.

[47] J. Huo, M. Wei, Characterization and magnetic properties of nanocrystalline

nickel ferrite synthesized by hydrothermal method, Mater. Lett. 63 (2009) 1183–1184.
[48] R.H. Kodama, A.E. Berkowitz, J.E.J. McNiff, S. Foner, Surface Spin Disorder in $ {\mathrm{NiFe}}_{2}{O}_{4}$ Nanoparticles, Phys. Rev. Lett. 77 (1996) 394–397.
[49] S.-H. Lee, H.M. Cheong, N.-G. Park, C.E. Tracy, A. Mascarenhas, D.K. Benson, S.K. Deb, Raman spectroscopic studies of Ni–W oxide thin films, Solid State Ion. 140 (2001) 135–139.
[50] A.R. Neale, Y. Jin, J. Ouyang, S. Hughes, D. Hesp, V. Dhanak, G. Dearden, S. Edwardson, L.J. Hardwick, Electrochemical performance of laser micro-structured nickel oxyhydroxide cathodes, J. Power Sources 271 (2014) 42–47.
[51] K.P.O. Mahesh, D.-H. Kuo, Synthesis of Ni nanoparticles decorated SiO2/TiO2 magnetic spheres for enhanced photocatalytic activity towards the degradation of azo dye, Appl. Surf. Sci. 357 (2015) 433–438.
[52] D. Li, S. Komarneni, Microwave-Assisted Polyol Process for Synthesis of Ni Nanoparticles, J. Am. Ceram. Soc. 89 (2006) 1510–1517.
[53] D. Roy, S. Neogi, S. De, Mechanistic investigation of photocatalytic degradation of Bisphenol-A using MIL-88A(Fe)/MoS2 Z-scheme heterojunction composite assisted peroxymonosulfate activation, Chem. Eng. J. 428 (2022) 131028.
[54] F. Liu, J. Cao, Z. Yang, W. Xiong, Z. Xu, P. Song, M. Jia, S. Sun, Y. Zhang, X. Zhong, Heterogeneous activation of peroxymonosulfate by cobalt-doped MIL-53 (Al) for efficient tetracycline degradation in water: Coexistence of radical and non-radical reactions, J. Colloid Interface Sci. 581 (2021) 195–204.
[55] Z. Li, M. Wang, C. Jin, J. Kang, J. Liu, H. Yang, Y. Zhang, Q. Pu, Y. Zhao, M. You, Z. Wu, Synthesis of novel Co3O4 hierarchical porous nanosheets via corn stem and MOF-Co templates for efficient oxytetracycline degradation by peroxymonosulfate activation, Chem. Eng. J. 392 (2020) 123789.
[56] Z. Li, F. Wang, Y. Zhang, Y. Lai, Q. Fang, Y. Duan, Activation of peroxymonosulfate by $CuFe_2O_4$-$CoFe_2O_4$ composite catalyst for efficient bisphenol a degradation: Synthesis, catalytic mechanism and products toxicity assessment, Chem. Eng. J. 423 (2021) 130093.
[57] L. Jing, W. Yang, T. Wang, J. Wang, X. Kong, S. Lv, X. Li, R. Quan, H. Zhu, Porous boron nitride micro-nanotubes efficiently anchor $CoFe_2O_4$ as a magnetic recyclable catalyst for peroxymonosulfate activation and oxytetracycline rapid degradation, Sep. Purif. Technol. 290 (2022) 120925.